

A Bird's-Eye View on Ambient Infrasonic Soundscapes

den Ouden, Olivier F.C.; Smets, Pieter S.M.; Assink, Jelle D.; Evers, Láslo G.

DOI

[10.1029/2021GL094555](https://doi.org/10.1029/2021GL094555)

Publication date

2021

Document Version

Final published version

Published in

Geophysical Research Letters

Citation (APA)

den Ouden, O. F. C., Smets, P. S. M., Assink, J. D., & Evers, L. G. (2021). A Bird's-Eye View on Ambient Infrasonic Soundscapes. *Geophysical Research Letters*, 48(17), Article e2021GL094555. <https://doi.org/10.1029/2021GL094555>

Important note

To cite this publication, please use the final published version (if applicable).
Please check the document version above.

Copyright

Other than for strictly personal use, it is not permitted to download, forward or distribute the text or part of it, without the consent of the author(s) and/or copyright holder(s), unless the work is under an open content license such as Creative Commons.

Takedown policy

Please contact us and provide details if you believe this document breaches copyrights.
We will remove access to the work immediately and investigate your claim.

Geophysical Research Letters



RESEARCH LETTER

10.1029/2021GL094555

Key Points:

- Evanescent microbaroms and propagating microbaroms are measured on an infrasound bio-logger fitted to a Wandering Albatross
- A method is developed to reconstruct omnidirectional microbarom soundscapes in absolute values, which can account for both microbarom fields
- The method is used to quantify the probabilistic microbarom exposure of microbarometers

Supporting Information:

Supporting Information may be found in the online version of this article.

Correspondence to:

O. F. C. den Ouden,
olivier.den.ouden@knmi.nl





Citation:

den Ouden, O. F. C., Smets, P. S. M., Assink, J. D., & Evers, L. G. (2021). A bird's-eye view on ambient infrasonic soundscapes. *Geophysical Research Letters*, 48, e2021GL094555. <https://doi.org/10.1029/2021GL094555>

Received 26 MAY 2021

Accepted 11 AUG 2021

A Bird's-Eye View on Ambient Infrasonic Soundscapes

Olivier F. C. den Ouden^{1,2} , Pieter S. M. Smets^{1,2} , Jelle D. Assink¹ , and Láslo G. Evers^{1,2} 

¹R&D Department of Seismology and Acoustics, Royal Netherlands Meteorological Institute, De Bilt, The Netherlands,

²Department of Geoscience and Engineering, Delft University of Technology, Delft, The Netherlands

Abstract A method is introduced to reconstruct microbarom soundscapes in absolute values. The soundscapes are compared to remote infrasound recordings from infrasound array I23FR (Kerguelen Island) and *in situ* recordings by the INFRA-EAR, a biollogger deployed near the Crozet Islands. The reconstruction method accounts for all-acoustic contributions, divided into evanescent microbaroms (detectable directly above the source) and propagating microbaroms (detectable over long ranges). It is computed by integrating acoustic intensities over the ocean surface, convolved with the transfer function quantifying the propagation losses and propagation time. The reconstructed soundscapes are found within 2.7 dB for 85% of the measurements in the microbarom band of 0.1–0.3 Hz. Infrasonic soundscapes are essential for understanding the ambient infrasonic noise field and are a basic need for applications, such as atmospheric remote sensing, natural hazard monitoring, and verification of the Comprehensive Nuclear-Test-Ban Treaty.

Plain Language Summary Microbaroms are omnipresent sources of low-frequency, inaudible sound, that is, infrasound. They have a characteristic and continuous signature within the infrasound spectrum and are often classified as ambient noise. The microbarom signals can be divided into a direct signal, only detectable close by the source, and a propagating signal, which travels over large distances. Under noisy conditions, microbaroms can mask infrasonic signals of interest, such as infrasound from volcanoes or explosions. Insights in the ambient noise field improve natural hazards monitoring and the verification of the Comprehensive Nuclear-Test-Ban Treaty. In this study, a method for the reconstruction of the microbarom source field is introduced. The method reconstructs omnidirectional soundscapes in absolute numbers. This is a significant improvement to previous approaches, which accounted for the normalized loudest source region only. The reconstructed soundscapes are compared with microbarom recordings by microbarometer arrays and the INFRA-EAR, a miniature sensor deployed as a biollogger near the Crozet Islands. The comparison shows a statistical agreement for 85% of the time between the modeled and observed soundscapes.

1. Introduction

The Southern hemisphere is characterized by its sparsity of *in situ* atmospheric observations due to large ocean volumes and consequently limited landmass. Meteo-France maintains and operates meteorological measurement facilities at some of the French Sub Antarctic and Antarctic lands. The Southern Oceans weather forecasts benefits from those *in situ* facilities in combination with remote satellite data (ERA5 Reanalysis, 2017; Levy & Brown, 1991). This study discusses the measurement of atmospheric pressure perturbations and their variations. Those observations have shown to be valuable for studying both infrasound and gravity waves (Blanc et al., 2018; Hupe, 2019; Marlton et al., 2019). Such observations can be retrieved from microbarometer arrays that are part of the global International Monitoring System (IMS). The IMS is in place to verify the Comprehensive Nuclear-Test-Ban Treaty (CTBT; Marty, 2019), and globally monitors the infrasonic wavefield.

Deep oceanic ambient noise is globally the most omnipresent seismic and infrasound source. The sea state describes the energy of the ocean surface and is the driving force for four different seismo-acoustic wave contributions (Figure 1a). (a) Evanescent microbaroms at the ocean-air interface are a direct product of traveling ocean surface waves, unregarded the water depth nor bathymetry, and decays vertically (Hetzer et al., 2010; Waxler & Gilbert, 2006). (b) The primary microseisms are related to a traveling ocean waves as well; however, these are only generated at the seafloor whenever the surface wave is in phase with the ocean bathymetry (Ardhuin et al., 2015). Non-linear interaction of counter traveling ocean surface waves results

© 2021. The Authors.

This is an open access article under the terms of the [Creative Commons Attribution](https://creativecommons.org/licenses/by/4.0/) License, which permits use, distribution and reproduction in any medium, provided the original work is properly cited.

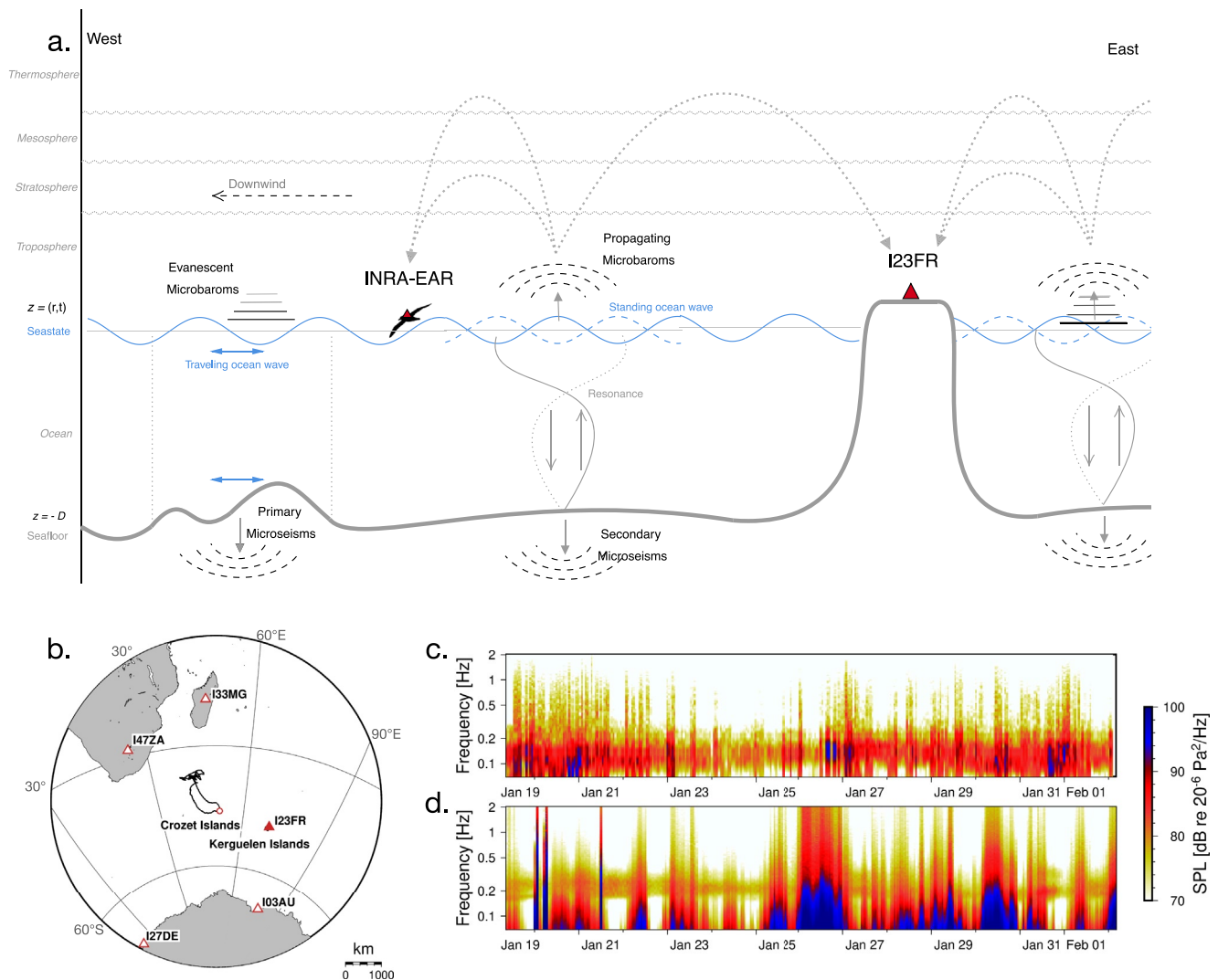


Figure 1. (a) A schematic overview of deep oceanic ambient noise. The blue signatures highlight the sea state and its products (traveling and standing ocean waves). The gray arrows indicate the generation of the acoustic components and the coupling to the interfaces. The black half-spheres show the radiation within the atmosphere and solid earth, from where a simplistic atmospheric propagation path is described. (b) The trip of the INFRA-EAR over the Southern Ocean. The triangles show IMS infrasound array locations. The circles indicate the start and end position of the trip. (c and d) Show the spectrogram of the recording by the INFRA-EAR and IMS array I23FR, respectively.

in standing ocean waves, causing the radiation of acoustic energy and resonance within the water column (Hasselmann, 1963; Longuet-Higgins, 1950). At the interfaces of the water column, acoustic energy is radiated into the atmosphere (c) propagating microbaroms (Brekovskikh, 1973) and down into solid seafloor (d) secondary microseisms (Longuet-Higgins, 1950).

Propagating microbaroms are often received at distant infrasound arrays and typically peak around 0.2 Hz (Campus & Christie, 2010). Various studies have focused on comparing microbarom simulations and distant IMS array observations (De Carlo, Hupe, et al., 2020; Landes et al., 2012; Vorobeve et al., 2020). Such studies are hampered by the relatively large distance of the arrays to the microbarom source regions, which is often largely spread out ($\sim 10,000 \text{ km}^2$). Typically, array processing techniques are applied to detect the dominant acoustic signal and direction-of-arrival in a given time segment and frequency band. Therefore, only the resolved direction and amplitude of this most dominant microbarom observation is compared with microbarom models. However, Assink et al. (2014) and Smets and Evers (2014) showed that multiple spatially distributed sources within the same time segment and frequency could occur.

In this study, atmospheric *in situ* and remote measurements of microbaroms within the Southern Ocean are obtained by, respectively, the “Infrasound, and Environmental Atmospheric data Recorder” (INFRA-EAR; den Ouden et al., 2021) and IMS array I23FR (Kerguelen Island). The INFRA-EAR is a multidisciplinary sensor platform for the monitoring of geophysical parameters. It has been fitted to the Southern Ocean’s largest seabirds, the Wandering Albatross (*Diomedea exulans*). During foraging trips, an albatross can fly thousands of kilometers away from its nest. Throughout the 2020 foraging trips, 25 INFRA-EARs have flown over the Southern Ocean to collect geophysical data. Furthermore, the INFRA-EARs are used to investigate the extent of infrasound and weather patterns in the navigation decisions by Wandering Albatrosses (Clay et al., 2020; Zeyl et al., 2020). The INFRA-EARs have collected a total of 115 h of absolute and differential pressure data while traveling over 42,184 km.

High-resolution array processing techniques to resolve spatially distributed infrasound sources, for example, CLEAN beamforming (den Ouden et al., 2020), cannot be applied to the INFRA-EAR observations. This is because the individual INFRA-EARs exist beyond the required aperture for beamforming (Evers, 2008). Instead, a method is developed to derive the different contributions of the microbarom field that are measured by the INFRA-EAR and I23FR array.

This article is organized as follows: Section 2 discusses the microbarom observations near the Crozet Islands. In Section 3, a reconstruction method that considers the contributions of multiple microbarom sources around an infrasound sensor is introduced. The comparison between the reconstructed microbarom soundscapes and the observations is described in Section 4, which is summarized and discussed in the final section.

2. Microbarom Observations Near Crozet Islands

2.1. The INFRA-EAR: *In Situ* Infrasound Measurements

The INFRA-EAR is a multidisciplinary sensor platform for monitoring geophysical parameters (den Ouden et al., 2021). The platform uses digital microelectromechanical sensors and monitors concurrently various geophysical parameters, such as differential and absolute pressure. The battery lifetime depends on the sensors power consumption. Therefore, the sensors are not continuously recording during a trip, as the battery lifetime is limited. The differential pressure sensor (KNMI mini-MB) is activated in bursts of 5 min, each hour, with a sampling frequency of 10 Hz to measure the small pressure perturbations. den Ouden et al. (2021) stated that the KNMI mini-MB measures on the order of 10^{-2} Pa and is biased by 2 ± 1 dB at frequencies below 1 Hz. The logger provides a GPS timestamp per sample point and a position every 15 min.

The INFRA-EAR is fitted to wandering albatrosses at the Crozet Islands. The average trip takes approximately 15 days while traveling thousands of kilometers. The recordings of the INFRA-EAR occur directly above the sea surface, ~ 5 m (Richardson et al., 2018; Supporting Information S1).

2.2. IMS Array I23FR: Remote Infrasound Observations

Infrasound array I23FR is located at Kerguelen Island, $\pm 1,500$ km from the INFRA-EAR recordings. Due to the INFRA-EAR’s proximity to I23FR, it is reasonable to assume that the differential pressure recordings show similar characteristics. The I23FR array has an aperture of ± 500 m and is divided into five triplets of MB 2005 microbarometers (Ponceau & Bosca, 2010) with an inter spacing of ± 100 m. This array, however, is often excluded from scientific studies due to adverse weather conditions and strong westerly winds (Brown et al., 2014). The array continuously measures small pressure perturbations with a sampling frequency of 20 Hz.

2.3. Comparison Between the Microbarom Measurements

The *in situ* recordings of the INFRA-EAR are compared with remote observations at I23FR. Both are analyzed in the frequency domain by means of spectra and interpreted as coherent infrasound and incoherent pressure fluctuations due to the wind and turbulence (Raspet et al., 2019). The INFRA-EARs recordings

are transferred into a power spectral density (PSD; Welch, 1967), which are combined in a spectrogram. The I23FR recordings are zero-delayed processed, and as well transferred into PSD's and combined in a spectrogram.

Within this study, recordings of one INFRA-EAR's trip have been compared with I23FR observations (Figures 1c and 1d, respectively). While significant overlap is noted, the INFRA-EAR spectra include low frequencies that do not appear to be measured by I23FR. This discrepancy can be understood when reconstructing the microbarom infra-soundscape, as will be done in the next section.

3. Microbarom Infra-Soundscape Reconstruction

The most omnipresent infrasound sources are deep oceanic microbaroms, for which several source models have been published in literature (Brekovskikh, 1973; De Carlo, Ardhuin, & Le Pichon, 2020; Waxler et al., 2007). From the order expansion of the equations of fluid mechanics (Waxler & Gilbert, 2006), it follows that the acoustic response of microbaroms can be described with an evanescent and propagating component.

These components are derived from the sea state ($\xi(x, t)$ at position x at time t), describing the excitement and energy within the ocean due to surface winds. The sea state is expressed as a slowly varying two-dimensional stochastic wave variance spectrum F :

$$\xi(r, t) = F(f_w, \phi) \quad (1)$$

where f_w indicates the ocean wave frequency, and ϕ the direction, F describes the distribution of the wave variance for a steady-state by superposition of linear waves over different frequencies and directions. The Hasselman (1963) integral is related to this spectrum and is defined by the superposition of linear waves to the statistical density spectrum of ideal counter-propagating ocean surface waves by:

$$\mathcal{H}(f_w) = \int_0^{2\pi} F(f_w, \phi) F(f_w, \phi - \pi) d\phi \quad (2)$$

This vibrating interface acts as a membrane, causing a velocity potential inducing a pressure oscillation near this interface. Acoustic energy is radiated into the ocean, propagating through the water column, and outwards into the atmosphere. Interference between the downward and upward propagation of signals within the water column may lead to resonance. The resonance terms within the water column for the finite ocean depths are described by the coefficients A , B , and C :

$$A = \mathcal{R}^2 \cos^2(\phi) + \sin^2(\phi)$$

$$B = \cos^2(\phi) + \mathcal{R}^2 \sin^2(\phi)$$

$$C = (1 - \mathcal{R}^2) \sin(\phi) \cos(\phi)$$

with $\mathcal{R} = (\rho_w c_w) / (\rho_b c_b)$, which is reflection coefficient obtained from the continuity of pressure between water (w) and the solid sea floor (b). ρ and c are the density and speed of sound within the ocean (w) and bedrock (b). Whenever $\mathcal{R} = 1$, such that the resonance terms become $A/B = 1$ and $C = 0$, the microbarom source model assumes an infinitely deep ocean. The water column's resonance depends on the acoustic wavelength λ_w and the ocean depth D (bathymetry), assuming microbaroms radiate on a direct path between the surface and solid seafloor without spreading. The amount of interference patterns depends on the phase difference $\phi = 2\pi D / \lambda_w$ between the signals. Vertical resonance occurs when $D / \lambda_w = 1/4 + n/2$ for any integer n (Smets, 2018).

The evanescent microbaroms directly correspond to a traveling ocean surface wave. Indifferent of the ocean depth nor bathymetry. This evanescent component does not radiate and decays vertically (Hetzer et al., 2010; Waxler & Gilbert, 2006), and can only be resolved directly above the source area. The propagating microbaroms are a result of the standing surface wave (Hasselman, 1963; Longuet-Higgins, 1950) and depends on the ocean depth and bathymetry (Brekovskikh, 1973; Waxler et al., 2007). This propagating component does radiate, propagates over large distances, and is measured at distant ground-based infrasound arrays.

The monitored microbarom spectrum by the IMS typically peak around 0.2 Hz (Campus & Christie, 2010), which are the propagating microbaroms. The sea state producing these signals peaks at 0.1 Hz (Waxler & Gilbert, 2006), as the evanescent component.

For the construction of both microbarom signals, the ECMWF ERA5 HRES ocean wave model has been used (2DFD), consisting of 30 steps for frequency and 24 for direction, respectively. This 2DFD reanalysis is coupled to the atmosphere model, which allows interaction between the ocean waves and the surface winds (Haiden et al., 2018). This 2DFD reanalysis has an hourly output, with a spatial resolution of 0.36°.

3.1. Integrating Microbarom Source Power

Evanescent microbaroms are detectable directly above the source, whereas the propagating microbaroms are detectable over long ranges. The total acoustic power is a summation of all-acoustic contributions. It is computed by integrating the computed acoustic intensities over the ocean surface (Pierce, 2019), convolved with the transfer function quantifying the propagation losses and propagation time.

$$\begin{aligned}\mathcal{P}_{av}(f, t_{\text{obs}}, x_r) &= \sum_i \mathcal{P}_{av,i}(f, t_{\text{obs}}, x_r) \\ &= \underbrace{\iint_{S_r} \mathcal{P}_1(f, t_{\text{obs}}, x_r) dS_r}_{\text{Evanescent microbaroms}} \\ &\quad + \underbrace{\sum_i \iint_{S_i} \mathcal{P}_2(f, t_0(\tau), x_s) \times G(f, t_{\text{obs}} - \tau, x_s, x_r) dS_i}_{\text{Propagating microbaroms}}\end{aligned}\quad (3)$$

In Equation 3, \mathcal{P}_{av} is the average acoustic power over frequency f received at t_{obs} and receiver position x_r , which has radiated from the area S_i , which encloses the i th sound source. \mathcal{P}_{av} can be subdivided into an evanescent (\mathcal{P}_1) and propagating component (\mathcal{P}_2). The source area of the evanescent component (S_r) is derived within Supporting Information S1. The propagation factor of the second-order component is presented by G , which describes the attenuation function and the propagation time (τ) between source (t_0, x_s) and receiver (t_{obs}, x_r). This integration holds when the total surface S encloses the entire collection of individual surfaces from sources S_i . Note that the value of $\mathcal{P}_{av,i}$ is construed to be dependent on the strength of other nearby sources. These assumptions apply if the source is multiple wavelengths apart from the other sources within S_i (Pierce, 2019).

3.2. Evanescent Microbaroms

It has been theorized that the evanescent microbaroms are detectable by measurements just above the source region. Such measurements are limited (Bowman & Lees, 2018), and do not mention nor adjudge evanescent microbaroms. The amplitude of the received evanescent microbaroms depends on the initial amplitude and the vertical decay between source and receiver.

3.2.1. Source Model

The acoustic power of the evanescent microbaroms has been derived by Waxler and Gilbert (2006) as:

$$\mathcal{P}_1(f_a) \sim \rho_a c_a^2 \frac{2\pi f_0^2}{k_0 c_a} \frac{2\pi f_0 \bar{F}(f_w)}{c_a} \quad (4)$$

where a and w represents the media of propagation (i.e., the atmosphere (a) and water(w)). \bar{F} is the integral of F over all direction, resulting in the sea mean energy spectrum. k_0 represents the wavenumber at the peak frequency f_0 of the spectrum.

3.2.2. Vertical Decay

The energy of evanescent microbaroms decays vertically (Waxler & Gilbert, 2006). Therefore this acoustic component is negligible outside its source region. The attenuation is rather simple and can be expressed as:

$$A(x_r, z) = e^{-k_z \cdot z} \quad (5)$$

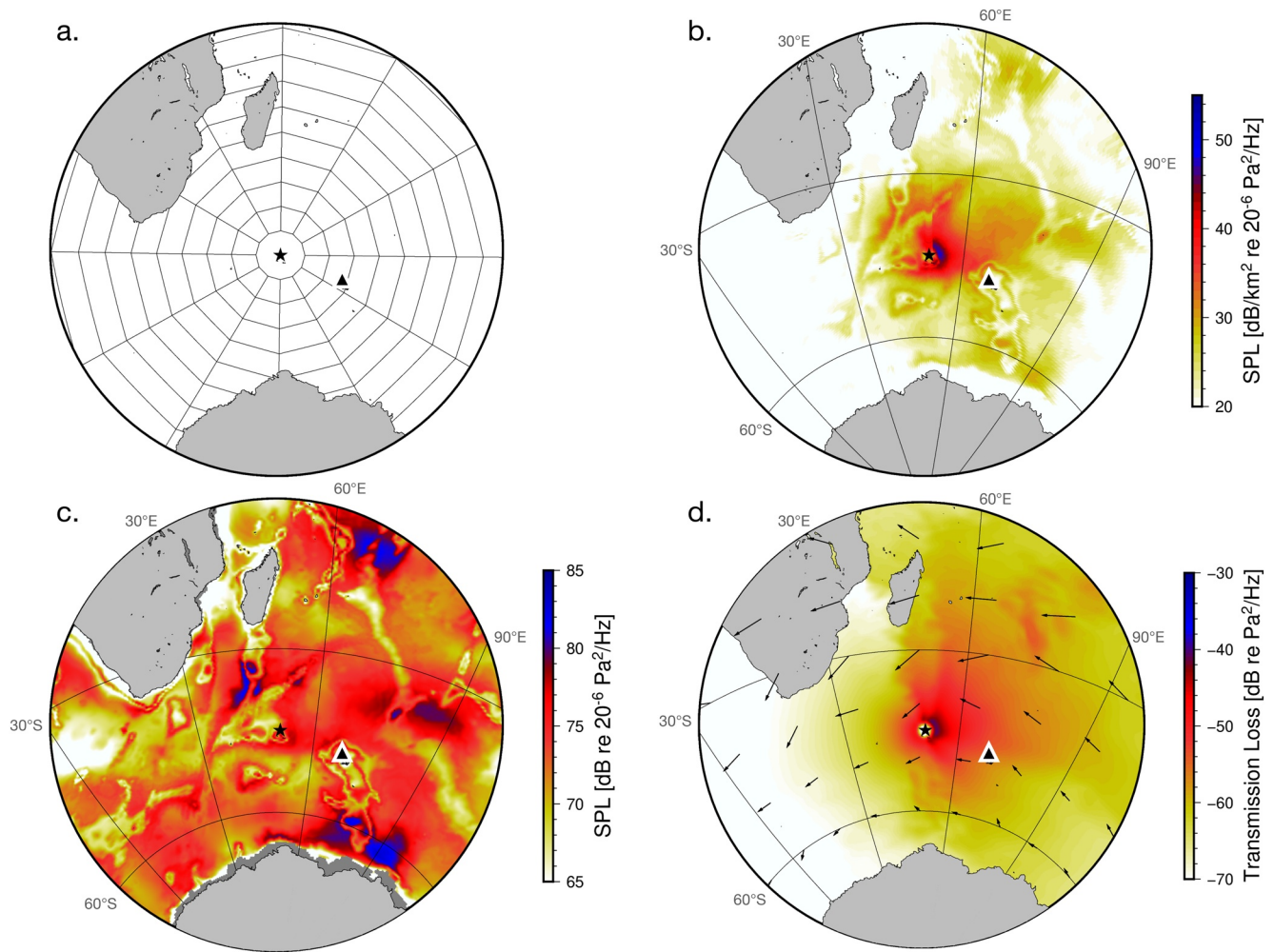


Figure 2. The reconstruction of the synthetic microbarom source model integrated between 0.1 and 0.3 Hz for illustration. (a) The stereographic polar grid, where the star indicates the origin and so the GPS position of the INFRA-EAR on 2020-01-19T14:00 UTC. (b) The reconstructed acoustic power per area in the surrounding of the INFRA-EAR. (c) The microbarom source model according Waxler et al. (2007), implemented by Smets and Evers (2014) using the ERA5 HRES 2DFD reanalysis. (d) The transmission loss, following Le Pichon et al. (2012) and Tailpied et al. (2016), from every grid cell toward the sensors GPS position, using the ERA5 HRES reanalysis. The vectors indicate the wind direction and speed. The triangle indicates the location of I23FR at Kerguelen Islands. Similar analysis has been performed for I23FR, by positioning the infrasound array as origin of the stereographic polar grid.

where z indicates the receiver's altitude, and k_z the corresponding vertical wave number (Supporting Information S1).

3.3. Propagating Microbaroms

As outlined in Equation 3, the integration of the propagating microbaroms is more complex since the attenuation due to long-range propagation of distant source has to be taken into account. This is numerically implemented by spanning a local polar stereographic grid, with the sensor as the polar position (Figure 2a). The computation of acoustic power, with accounted propagation effects, has been interpolated over this stereographic grid. It has been weighted for the variable surface area dS , as this grows with increasing distance as a function of azimuth. Figure 2b shows the corrected and interpolated microbarom source regions around the INFRA-EAR (50°E, 45°S) at 2020-01-19T14:00 UTC. This figure defines the acoustic power per area, which potentially has been recorded by the INFRA-EAR.

3.3.1. Source Model

The propagated microbarom source model is described by Waxler et al. (2007) and implemented and verified by Smets and Evers (2014). This source strength model is based on the work by Longuet-Higgins (1950), Brekovskikh (1973), and Waxler and Gilbert (2006). Waxler et al. (2007) describes the source regions as an isotropic source above an ocean with finite depth:

$$\mathcal{P}_2(f_a) = 4g^2\pi^4 f_a^3 \mathcal{H}(f_w) \frac{\rho_a^2}{c_a^2} \left(\frac{9g^2}{4\pi^2 c_a^2 f_a^2} + \frac{c_a^2}{c_w^2} \frac{A}{B} + \frac{3g}{2\pi c_w f_a} \frac{C}{B} \right) \quad (6)$$

where $f_a (= 2f_w)$ is the acoustic frequency. \mathcal{H} indicates the Hasselmann (1963) integral, which describes the standing wave density spectrum. A , B , and C are the describing resonance terms within the water column for the finite ocean depths. Figure 2c shows the microbarom source regions for 2020-01-19T14:00 UTC.

3.3.2. Long-Range Propagation

Infrasound can propagate over large distances facilitated by acoustic waveguides, formed between the Earth surface and atmospheric layers (Figure 1a). These waveguides change with time and location. The effective sound speed approximates the combined effect of wind and temperature on infrasound propagation in a horizontally layered atmosphere (c_{eff}), which is defined as the sum of the adiabatic sound speed (c_T) and the wind in the direction of propagation (Drob, 2019). The effective speed of sound ratio ($c_{\text{eff, ratio}}$) is a practical measure to quantify favorable ground-to-ground ducting conditions. An effective sound speed ratio near to or greater than 1 is indicative of whether infrasound can refract back to the Earth surface.

Various methods have been developed to accurately simulate infrasound in realistic atmospheres (Waxler & Assink, 2019), such as parabolic equation (PE) methods. Within this study, the empirical formation by Tailpied et al. (2016) is used, which extends the original methodology by Le Pichon et al. (2012) for a range-dependent atmosphere. The empirical relation according Le Pichon et al. (2012) represents the average of a large number of representative PE runs and is formulated as:

$$A(x_r, x_s) = \frac{1}{r} 10^{\frac{\alpha(f)r}{20}} + \frac{r^{\beta(f, c_{\text{eff, ratio}})}}{1 + 10^{\frac{\delta - r}{\sigma(f)}}} \quad (7)$$

where α, β, δ , and σ are the dissipation of the direct wave, the geometrical spreading and dissipation of both the stratospheric and thermospheric paths, the width of the shadow zone, and is a scaling distance controlling the strength of the attenuation in the shadow zone. Equation 7 includes both the classical and relaxation losses, which are frequency-dependent and modeled using vertical profiles of temperature, density, and the concentration of atmospheric gasses (Sutherland & Bass, 2004). The empirical relation, which account for lateral heterogeneity (Tailpied et al., 2016) between receiver position x_r and source x_s at a reference distance of 1 km, is formulated as:

$$A(x_r, x_s) = \prod_i \frac{A_{x_r, i+1, x_s}^{i+1}}{A_{x_r, i, x_s}^{i+1}} \quad (8)$$

Figure 2d shows the transmission loss for propagation from each grid cell toward the INFRA-EAR's GPS position at 2020-01-19T14:00 UTC, integrated between 0.1 and 0.3 Hz for illustration. This highlights the potential source regions that can be recorded and the associated attenuation along the source- receiver path. In addition, it is shown that the propagation is effective downwind, as is illustrated by the stratospheric wind direction (vectors).

The source contributions of the microbarom model have been compensated for the attenuation along its propagation path toward the INFRA-EAR at the time of recording. However, this only describes the attenuation along the propagation path. In order to account for significant propagation times between source region and receiver, each grid cell is evaluated at the model time t_m that is, nearest to the observation time t_{obs} minus the propagation time τ , that is, $t_m = q(t_{\text{obs}} - \tau)$, where q represents the rounding to the nearest model time. The simulated soundscape consists of microbarom source regions that exist throughout different hours of the day. The stratospheric propagation has been characterized by a celerity range of 0.25–0.31 km/s, which is directly correlated to the $c_{\text{eff, ratio}}$. Whenever the stratospheric propagation is not feasible, thermospheric

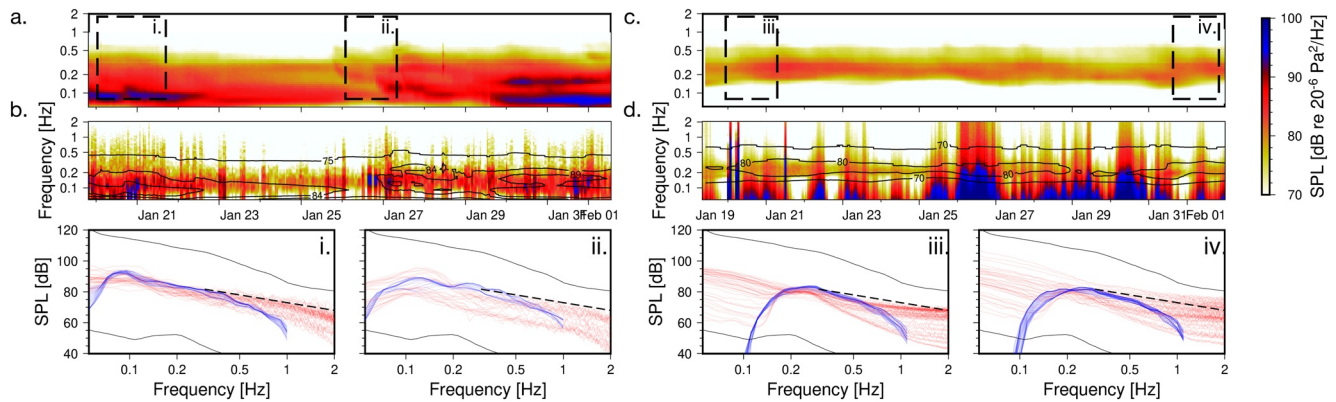


Figure 3. The comparison between the synthetic microbarom spectra (a and c) and the recorded infrasound by the INFRA-EAR (b) and I23FR (d). Overlaying the recorded spectrograms by contour lines of the synthetics in (b) and (d) allows a visual comparison. (i), (ii), (iii), and (iv) show the PSD of the synthetic (blue) and observations (red) for a specific time. The gray lines indicate the high and low global IMS noise levels (Brown et al., 2014), whereas the dotted line highlights the $f^{-5/3}$ slope expected for turbulence (Chunchuzov & Kulichkov, 2019).

propagation is assumed with a range of 0.21–0.25 km/s (Assink et al., 2012; Evers & Haak, 2007; Vergoz et al., 2019).

4. Comparison of *In Situ* Observations and Soundscapes

The route of the INFRA-EAR, as mounted on an albatross, has been simulated using the method outlined in Section 3 to compare model and observations. The measurement of the INFRA-EAR occurs directly above the sea surface (~5 m; Richardson et al., 2018). Therefore, a synthetic sound spectrum has been created to obtain a spectrogram for each frequency within the evanescent and propagating microbarom model. Figure 3a shows the synthetic spectrogram for the INFRA-EAR, while Figure 3b shows the recorded spectrogram by the INFRA-EAR. For the same period, the analysis has been performed on I23FR, a distant (~1,500 km) ground-based infrasound array (Green et al., 2012; Figures 3c and 3d). The synthetic spectrograms' contour lines are plotted over the recorded spectrograms for comparison. The panels below the spectrograms highlight specific recording periods and directly compare the observed (red) and synthetic spectra (blue). The microbarom spectral information of recordings and observations are found to be in close agreement. The structure of the overlaid contour lines in Figures 3b and 3d are in conformance with the recorded data. Remind that I23FR is a ground-based array and thus only records propagating microbaroms. The INFRA-EAR, however, can observe both the evanescent and the propagating microbaroms (Supporting Information S1), explaining the low-frequency contents down to 0.1 Hz.

Figures 4a and 4c show the integrated acoustic power summation (Equation 3) between 0.1 and 0.3 Hz for both INFRA-EAR's and I23FR's synthetic and recorded spectra. The integrated amplitudes of the observations (red) align with the integrated total acoustic power summation of the synthetic microbarom model (black). Based on the mean absolute error (MAE) and bias between the model and observations, the relative frequency for which the bias is below the MAE, is 2.7 dB for 85% of the INFRA-EAR recording (Supporting Information S2; NOAA Meteorological Development Laboratory, 2021).

Figures 4b and 4d shows the statistical reconstruction of the total acoustic power summation over the stereographic polar grid. The percentile of total power has been determined per distance away from the INFRA-EAR and I23FR, respectively. The computation shows that the near-evanescent component needs to be taken into account for the INFRA-EAR and not for I23FR. Furthermore, it suggests that 95% of the microbarom source field contributes up to 2,000 km from the INFRA-EAR's recording. Source contributions from outside this region are minimal. Since the reconstruction around an infrasound sensor depends critically on the characteristics of the microbarom source model and propagation conditions, it is expected that the size of the contributing source region will vary as a function of geographical location and time. For example, array-specific cumulative probability distributions could be constructed for global IMS infrasound arrays to quantify the array's microbarom exposure and hence the noise levels.

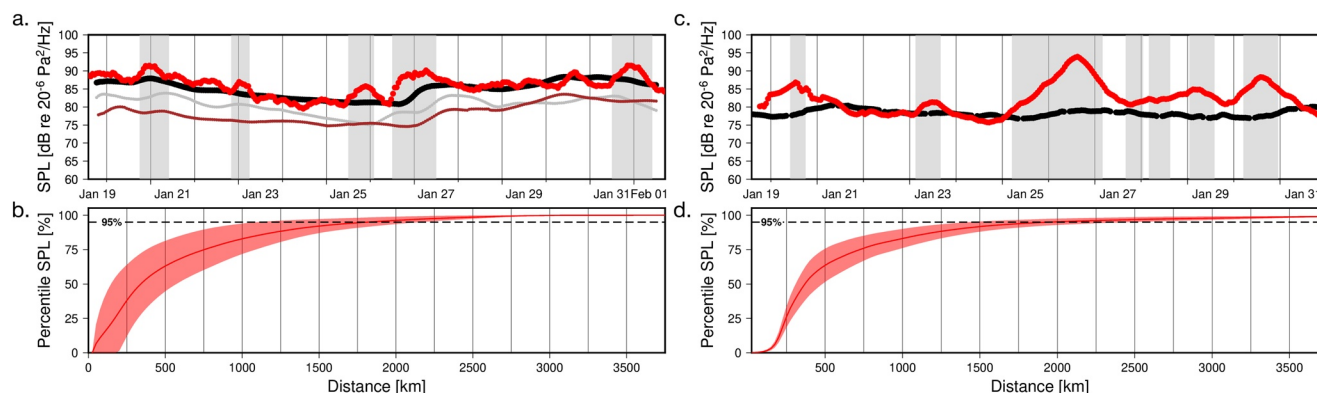


Figure 4. (a) and (c) The total acoustic power summation of the reconstructed microbarom source model (black) integrated between 0.1 and 0.3 Hz and the measured infrasound by the INFRA-EAR (a, red) and I23FR (c, red). The total power can be divided into an evanescent (gray line) and propagating (brown line) microbarom contribution. The gray areas indicate periods when the recorded power spectra follow the $f^{-5/3}$ slope. (b) The cumulative probability of the percentile SPL per distance from the receiver.

5. Discussion and Conclusion

In this study, a method has been introduced for the reconstruction of microbarom soundscapes. This method accounts for evanescent and propagating microbaroms of multiple source contributions in an infrasound sensor's vicinity. The method generates synthetic spectra in absolute numbers, which agree with infrasound recordings by a mobile logger deployed in the middle of the Southern Ocean and a distant IMS infrasound array. The presented soundscapes rely on several approximations related to (a) the source model and (b) the assumptions made in the propagation modeling. However, the methodology is modular and allows plugging in different microbarom models, ocean wave models, and propagation models.

The microbaroms source region model, evanescent and propagating microbaroms, as described by Waxler and Gilbert (2006) and Waxler et al. (2007) has been used within this study as source intensity input for the reconstructed soundscapes and has been computed using the ERA5 2DFD model of the ECMWF. Recently, De Carlo, Arduin, and Le Pichon (2020) have studied the propagating microbarom source radiation pattern. This work concluded that including finite-depth ocean effects in the model is especially relevant for near-vertical propagation (Brekovskikh, 1973). Here, synthetic soundscapes are compared with *in situ* measurements of the INFRA-EAR, which record both the evanescent and propagating microbaroms. It is therefore relevant to account for the near-vertical propagation of the propagating microbaroms. The source model by Waxler et al. (2007) includes these effects and therefore has been used within this study.

Furthermore, the assumptions made in the propagation model influence the soundscapes. The empirical formulation of sound propagation by Tailpied et al. (2016) and Le Pichon et al. (2012), is modeled along the great circle path from source to the receiver only, neglecting out-of-plane propagation effects. This model can be used to approximate propagation losses in atmospheres with a dual (stratospheric-thermospheric) duct and neglects tropospheric ducting. A different approach could involve using a 3D ray-theory model cast in spherical coordinates (Blom, 2019; Smets, 2018), to quantify propagation losses. The use of formal propagation models requires atmospheric specifications from the ground to the upper atmosphere. As upper atmospheric specifications are typically limited to climatologies, this has implications for the accuracy of thermospheric returns (Assink et al., 2012; Drob, 2019).

Although various assumptions have been made, the close agreement between the model and observations shown in Figures 3 and 4 show that the proposed methodology can be used to reconstruct the microbarom soundscape around an infrasound sensor. Both comparisons, integrated and spectral, between soundscapes and recordings show a near-perfect agreement for frequency and amplitude. For example, the agreement between the integrated soundscapes and recordings is 2.7 dB for 85% off the time (Figure 4). Despite the agreement, some significant differences between model and observations stand out. The measured power is sometimes higher than predicted by the soundscape. It should be recalled that the synthetic soundscapes describe the radiated microbarom power that is, predicted from the modeled ocean wave spectra. It

is conceivable that local noise from wind and turbulence could have affected the measurements at intervals, which cause a discrepancy between model and observation, due to higher noise levels at the receiver (Marty, 2019; Rasset et al., 2019). When comparing Figure 4a with the barometric pressure measurements (Supporting Information S3), it is shown there is a strong barometric pressure gradient whenever a difference occurs between the microbarom model and observation. Barometric pressure gradients are often associated to higher winds and local turbulence, that is, higher noise conditions. Figure 3i shows the INFRA-EAR's acoustic power spectra compared to the synthetic power spectra around 2020-01-21. The dotted line in the Figure 3 indicates the $f^{-5/3}$ slope, which is typical for turbulence in the atmospheric boundary layer (Bacmeister et al., 1996; Chunchuzov & Kulichkov, 2019; Gossard & Hooke, 1975). Note that the power spectra of the INFRA-EAR follow this slope from 0.2 to 1 Hz. The gray areas in Figures 4a and 4c indicate the periods when the recorded power spectra follow the $f^{-5/3}$ slope. When the incoherent noise levels are high due to wind, acoustic signals can be masked and remain undetected.

The presented soundscapes give insight into how much various source regions contribute to the total acoustic power measured in the microbarom band. Earlier studies have been limited to analyzing normalized microbarom amplitudes, that is, no absolute microbarom power values. Furthermore, earlier work focused on the maximum contribution of a specific region rather than considering the field to distribute multiple source contributions based on directional data processing. Nonetheless, Assink et al. (2014) showed that multiple spatially distributed sources within the same time segment and frequency could occur. Those can be resolved by applying high-resolution data-processing techniques (den Ouden et al., 2020). However, the entire microbarom source field contributes and influences the total acoustic power. The application of this reconstruction is essential in understanding the infrasonic wavefield, the ambient noise field, and for remote sensing of the atmosphere. The analysis shown in Figure 3 leads to a better understanding of microbaroms' contributions to array recordings. In conclusion, the reconstruction of microbarom spectra with absolute numbers, instead of normalized values, improves the knowledge in the global infrasonic background noise and compares infrasound array observations with model outputs. This new knowledge contributes to a better verification of the CTBT and a better applicability of infrasound as a remote sensing technique for the upper atmosphere. Moreover, only a few studies have considered evanescent microbaroms. The recordings, analysis, and comparison of the evanescent microbarom component within this study is a direct product of the sea-state and can be used by oceanographers for monitoring purposes.

Acknowledgments

The authors would like to thank Mathieu Basille, Susana Clusella-Trullas, Thomas Clay, Dominique Filippi, Rocío Joo, Lucia Martin Lopez, Sam Patrick, Timothee Poupart, Henri Weimerskirch, and Jeff Zeyl for their collaboration on the development of the INFRA-EAR and the 2020 field campaign. In addition, many thanks to the Institut Polaire Français Paul Emile Victor (IPEV, program 109) and the Terres Australes and Antarctique Françaises (TAAF), which provided logistical and financial support for the field campaign. The INFRA-EAR data used within this study is FAIR according to the AGU guidelines and can be accessed via (den Ouden, 2021). The ECMWF ERA5 model data for reconstructing infrasonic soundscapes is available via (ERA5 Reanalysis, 2017). O.F.C. den Ouden and Jelle D. Assink are funded by a Human Frontier Science Program Young Investigator Grant (SeabirdSound—RGY0072/2017). Pieter S. M. Smets and Láslo G. Evers's contributions are funded through a VIDI project from the Netherlands Organization for Scientific Research (NWO), Project 864.14.005. The authors are grateful for helpful reviews by the Editor Germán Prieto and reviewers Roger Waxler and Daniel Bowman.

Data Availability Statement

The authors thank the CTBTO and station operators for the high quality of IMS data and products. IMS data can be accessed through the vDEC (see <https://www.ctbto.org/specials/vdec/>) by requesting data after filling out the necessary forms.

References

- Arduhin, F., Gualtieri, L., & Stutzmann, E. (2015). How ocean waves rock the earth: Two mechanisms explain microseisms with periods 3 to 300 s. *Geophysical Research Letters*, 42(3), 765–772. <https://doi.org/10.1002/2014gl062782>
- Assink, J., Waxler, R., & Drob, D. (2012). On the sensitivity of infrasonic traveltimes in the equatorial region to the atmospheric tides. *Journal of Geophysical Research*, 117(D1), D01110. <https://doi.org/10.1029/2011jd016107>
- Assink, J., Waxler, R., Smets, P., & Evers, L. (2014). Bidirectional infrasonic ducts associated with sudden stratospheric warming events. *Journal of Geophysical Research: Atmospheres*, 119(3), 1140–1153. <https://doi.org/10.1002/2013jd021062>
- Bacmeister, J. T., Eckermann, S. D., Newman, P. A., Lait, L., Chan, K. R., Loewenstein, M., et al. (1996). Stratospheric horizontal wavenumber spectra of winds, potential temperature, and atmospheric tracers observed by high-altitude aircraft. *Journal of Geophysical Research*, 101(D5), 9441–9470. <https://doi.org/10.1029/95jd03835>
- Blanc, E., Ceranna, L., Hauchecorne, A., Charlton-Perez, A., Marchetti, E., Evers, L. G., et al. (2018). Toward an improved representation of middle atmospheric dynamics thanks to the arise project. *Surveys in Geophysics*, 39(2), 171–225. <https://doi.org/10.1007/s10712-017-9444-0>
- Blom, P. (2019). Modeling infrasonic propagation through a spherical atmospheric layer—Analysis of the stratospheric pair. *Journal of the Acoustical Society of America*, 145(4), 2198–2208. <https://doi.org/10.1121/1.5096855>
- Bowman, D. C., & Lees, J. M. (2018). Upper atmosphere heating from ocean-generated acoustic wave energy. *Geophysical Research Letters*, 45(10), 5144–5150. <https://doi.org/10.1029/2018gl077737>
- Brekovskikh, L. (1973). Waves in layered media. In: B. Alexander Auld, (Ed.), *Acoustic fields and waves in solids* (Chap. 1, p. 449). New York: Academic Press.
- Brown, D., Ceranna, L., Prior, M., Mialle, P., & Le Bras, R. J. (2014). The IDC seismic, hydroacoustic and infrasound global low and high noise models. *Pure and Applied Geophysics*, 171(3–5), 361–375. <https://doi.org/10.1007/s00024-012-0573-6>

- Campus, P., & Christie, D. (2010). Worldwide observations of infrasonic waves. In A. Le Pichon, E. Blanc, & A. Hauchecorne (Eds.), *Infrasound monitoring for atmospheric studies* (pp. 185–234). Springer. https://doi.org/10.1007/978-1-4020-9508-5_6
- Chunchuzov, I., & Kulichkov, S. (2019). Internal gravity wave perturbations and their impacts on infrasound propagation in the atmosphere. In A. Le Pichon, E. Blanc, & A. Hauchecorne (Eds.), *Infrasound monitoring for atmospheric studies* (pp. 551–590). Springer. https://doi.org/10.1007/978-3-319-75140-5_16
- Clay, T. A., Joo, R., Weimerskirch, H., Phillips, R. A., Den Ouden, O., Basille, M., et al. (2020). Sex-specific effects of wind on the flight decisions of a sexually dimorphic soaring bird. *Journal of Animal Ecology*, 89(8), 1811–1823. <https://doi.org/10.1111/1365-2656.13267>
- De Carlo, M., Arduin, F., & Le Pichon, A. (2020a). Atmospheric infrasound generation by ocean waves in finite depth: Unified theory and application to radiation patterns. *Geophysical Journal International*, 221(1), 569–585.
- De Carlo, M., Hupe, P., Le Pichon, A., Ceranna, L., & Arduin, F. (2020b). Global microbarom patterns: A first confirmation of the theory for source and propagation. *Geophysical Research Letters*, 48(3), e2020GL090163.
- den Ouden, O. F. C. (2021). *OlivierdenOuden/GRL-INFRA-EAR-data: GRL INFRA-EAR data*. Zenodo. <https://doi.org/10.5281/zenodo.5138353>
- den Ouden, O. F. C., Assink, J. D., Oudshoorn, C. D., Filippi, D., & Evers, L. G. (2021). The infra-ear: A low-cost mobile multidisciplinary measurement platform for monitoring geophysical parameters. *Atmospheric Measurement Techniques*, 14(5), 3301–3317. <https://doi.org/10.5194/amt-14-3301-2021>
- den Ouden, O. F. C., Assink, J. D., Smets, P. S., Shani-Kadmiel, S., Averbuch, G., & Evers, L. G. (2020). Clean beamforming for the enhanced detection of multiple infrasonic sources. *Geophysical Journal International*, 221(1), 305–317.
- Drob, D. (2019). Meteorology, climatology, and upper atmospheric composition for infrasound propagation modeling. In A. Le Pichon, E. Blanc, & A. Hauchecorne (Eds.), *Infrasound monitoring for atmospheric studies* (pp. 485–508). Springer. https://doi.org/10.1007/978-3-319-75140-5_14
- ERA5 Reanalysis. (2017). *Research data archive at the National Center for Atmospheric Research, Computational and Information Systems Laboratory*. <https://doi.org/10.5065/D6X34W69>
- Evers, L. G., (2008). *The inaudible symphony: On the detection and source identification of atmospheric infrasound*, (PhD thesis). Delft University of Technology.
- Evers, L. G., & Haak, H. W. (2007). Infrasonic forerunners: Exceptionally fast acoustic phases. *Geophysical Research Letters*, 34(10), L10806. <https://doi.org/10.1029/2007gl029353>
- Gossard, E. E., & Hooke, W. H. (1975). *Waves in the atmosphere: Atmospheric infrasound and gravity waves-their generation and propagation*. Elsevier Science.
- Green, D., Matoza, R., Vergoz, J., & Le Pichon, A. (2012). Infrasonic propagation from the 2010 eyjafjallajökull eruption: Investigating the influence of stratospheric solar tides. *Journal of Geophysical Research*, 117(D21), D21202. <https://doi.org/10.1029/2012jd017988>
- Haiden, T., Janousek, M., Bidlot, J., Buizza, R., Ferranti, L., Prates, F., & Vitart, F. (2018). *Evaluation of ECMWF forecasts, including the 2018 upgrade*. European Centre for Medium Range Weather Forecasts.
- Hasselmann, K. (1963). A statistical analysis of the generation of microseisms. *Reviews of Geophysics*, 1(2), 177–210. <https://doi.org/10.1029/rg001i002p00177>
- Hetzer, C. H., Gilbert, K. E., Waxler, R., & Talmadge, C. L. (2010). Generation of microbaroms by deep-ocean hurricanes. In A. Le Pichon, E. Blanc, & A. Hauchecorne (Eds.), *Infrasound monitoring for atmospheric studies* (pp. 249–262). Springer. https://doi.org/10.1007/978-1-4020-9508-5_8
- Hupe, P. (2019). *Global infrasound observations and their relation to atmospheric tides and mountain waves*. Oxford University Press.
- Landes, M., Ceranna, L., Le Pichon, A., & Matoza, R. S. (2012). Localization of microbarom sources using the IMS infrasound network. *Journal of Geophysical Research*, 117(D6). <https://doi.org/10.1029/2011jd016684>
- Le Pichon, A., Ceranna, L., & Vergoz, J. (2012). Incorporating numerical modeling into estimates of the detection capability of the IMS infrasound network. *Journal of Geophysical Research*, 117(D5), D05121. <https://doi.org/10.1029/2011jd016670>
- Levy, G., & Brown, R. A. (1991). Southern hemisphere synoptic weather from a satellite scatterometer. *Monthly Weather Review*, 119(12), 2803–2813. [https://doi.org/10.1175/1520-0493\(1991\)119<2803:shswfa>2.0.co;2](https://doi.org/10.1175/1520-0493(1991)119<2803:shswfa>2.0.co;2)
- Longuet-Higgins, M. S. (1950). A theory of the origin of microseisms. *Philosophical Transactions of the Royal Society A*, 243(857), 1–35. <https://doi.org/10.1098/rsta.1950.0012>
- Marlton, G., Charlton-Perez, A., Harrison, G., & Lee, C. (2019). Calculating atmospheric gravity wave parameters from infrasound measurements. In A. Le Pichon, E. Blanc, & A. Hauchecorne (Eds.), *Infrasound monitoring for atmospheric studies* (pp. 701–719). Springer. https://doi.org/10.1007/978-3-319-75140-5_22
- Marty, J. (2019). The IMS infrasound network: Current status and technological developments. In A. Le Pichon, E. Blanc, & A. Hauchecorne (Eds.), *Infrasound monitoring for atmospheric studies* (pp. 3–62). Springer. https://doi.org/10.1007/978-3-319-75140-5_1
- NOAA Meteorological Development Laboratory. (2021). *Statistical verification scores* (2021). Retrieved from <https://vlab.ncep.noaa.gov/web/mdl/ndfd-verification-score-definitions>
- Pierce, A. D. (2019). *Acoustics: An introduction to its physical principles and applications*. Springer.
- Ponceau, D., & Bosca, L. (2010). Low-noise broadband microbarometers. In A. Le Pichon, E. Blanc, & A. Hauchecorne (Eds.), *Infrasound monitoring for atmospheric studies* (pp. 119–140). Springer. https://doi.org/10.1007/978-1-4020-9508-5_4
- Raspet, R., Abbott, J.-P., Webster, J., Yu, J., Talmadge, C., Alberts, K., II, et al. (2019). New systems for wind noise reduction for infrasonic measurements. In A. Le Pichon, E. Blanc, & A. Hauchecorne (Eds.), *Infrasound monitoring for atmospheric studies* (pp. 91–124). Springer. https://doi.org/10.1007/978-3-319-75140-5_3
- Richardson, P. L., Wakefield, E. D., & Phillips, R. A. (2018). Flight speed and performance of the wandering albatross with respect to wind. *Movement Ecology*, 6(1), 1–15. <https://doi.org/10.1007/s41116-017-0011-z>
- Smets, P. S. M. (2018). *Infrasound and the dynamical stratosphere: A new application for operational weather and climate prediction*. Delft University of Technology.
- Smets, P. S. M., & Evers, L. G. (2014). The life cycle of a sudden stratospheric warming from infrasonic ambient noise observations. *Journal of Geophysical Research: Atmospheres*, 119(21), 1208412. <https://doi.org/10.1002/2014JD021905>
- Sutherland, L. C., & Bass, H. E. (2004). Atmospheric absorption in the atmosphere up to 160 km. *Journal of the Acoustical Society of America*, 115(3), 1012–1032. <https://doi.org/10.1121/1.1631937>
- Tailpied, D., Pichon, A. L., Marchetti, E., Assink, J., & Vergnolle, S. (2016). Assessing and optimizing the performance of infrasound networks to monitor volcanic eruptions. *Geophysical Journal International*, 208(1), 437–448. <https://doi.org/10.1093/gji/ggw400>

- Vergoz, J., Le Pichon, A., & Millet, C. (2019). The Antares explosion observed by the USarray: An unprecedented collection of infrasound phases recorded from the same event. In A. Le Pichon, E. Blanc, & A. Hauchecorne (Eds.), *Infrasound monitoring for atmospheric studies* (pp. 349–386). Springer. https://doi.org/10.1007/978-3-319-75140-5_9
- Vorobeva, E., De Carlo, M., Le Pichon, A., Espy, P. J., & Näsholm, S. P. (2020). Microbarom radiation and propagation model assessment using infrasound recordings: A vespagram-based approach. *Annales Geophysicae Discussions*, 39, 515–531.
- Waxler, R., & Assink, J. (2019). Propagation modeling through realistic atmosphere and benchmarking. In: *Infrasound monitoring for atmospheric studies* (pp. 509–549). Springer. https://doi.org/10.1007/978-3-319-75140-5_15
- Waxler, R., Gilbert, K., Talmadge, C., & Hetzer, C. (2007). The effects of finite depth of the ocean on microbarom signals. In *8th International Conference on Theoretical and Computational Acoustics (ICTCA)*.
- Waxler, R., & Gilbert, K. E. (2006). The radiation of atmospheric microbaroms by ocean waves. *Journal of the Acoustical Society of America*, 119(5), 2651–2664. <https://doi.org/10.1121/1.2191607>
- Welch, P. (1967). The use of fast Fourier transform for the estimation of power spectra: A method based on time averaging over short, modified periodograms. *IEEE Transactions on Audio and Electroacoustics*, 15(2), 70–73. <https://doi.org/10.1109/tau.1967.1161901>
- Zeyl, J. N., den Ouden, O., Köppl, C., Assink, J., Christensen-Dalsgaard, J., Patrick, S. C., & Clusella-Trullas, S. (2020). Infrasonic hearing in birds: A review of audiometry and hypothesized structure–function relationships. *Biological Reviews*. 95(4), 1036–1054.